JACS
JOURNAL OF THE AMERICAN CHEMICAL SOCIETY

Communication

pubs.acs.org/JACS

# In-Situ Crystallization Route to Nanorod-Aggregated Functional ZSM-5 Microspheres

Bin Li,[†] Bo Sun,[†] Xufang Qian,[†] Wei Li,[†] Zhangxiong Wu,[†] Zhenkun Sun,[†] Minghua Qiao,[†] Mikel Duke,[‡] and Dongyuan Zhao*[,†]

[†]Department of Chemistry, Shanghai Key Laboratory of Molecular Catalysis and Innovative Materials and Laboratory of Advanced Materials, Fudan University, Shanghai 200433, P. R. China

[‡]Institute for Sustainability and Innovation, School of Engineering and Science, Victoria University, Melbourne, Vic 8001, Australia

Supporting Information

**ABSTRACT:** Herein, we develop a reproducible *in situ* crystallization route to synthesize uniform functional ZSM-5 microspheres composed of aggregated ZSM-5 nanorods and well-dispersed uniform $Fe_3O_4$ nanoparticles (NPs). The growth of such unique microspheres undergoes a NP-assisted recrystallization process from surface to core. The obtained magnetic ZSM-5 microspheres possess a uniform size (6−9 $\mu$m), ultrafine uniform $Fe_3O_4$ NPs (~10 nm), good structural stability, high surface area (340 $m^2/g$), and large magnetization (~8.6 emu/g) and exhibit a potential application in Fischer−Tropsch synthesis.

Zeolites as supports and catalysts have attracted interest due to their unique material properties[1] (e.g., high thermal stability, regular microporosity, unique shape selectivity, and intrinsic chemical activity) which can be widely applied in industrial operations, e.g., separation, catalysis, and adsorption.[2] Expanding the scope from pure zeolites to hybrid materials, by combining the properties of zeolites with other functional components (e.g., metals), significantly broadens the field of zeolite material capability.[3−5]

Recently, great efforts have been directed toward designing zeolites with desired functions. Conventionally, ion exchange or impregnation processes are the most common methods for introducing metal ions into zeolite pore channels.[6] However, these strategies are only effective for large-pore zeolites with pore size >0.7 nm, because small pores are not easily accessed.[7] An alternative route is to deposit guest species on the surface of zeolites through a physical or chemical process, which can endow a useful function.[8,9] Nevertheless, these guest materials deposited on the surface are typically too big or not well-dispersed throughout the zeolites, resulting in easy desquamation from catalysts and loss of function. Despite the success in demonstrating functional enhancements from these top-down methods, a bottom-up method based on *in situ* combination of zeolite precursors and guest species [metal ions or nanoparticles (NPs)] is pursued because of its facile and controllable synthesis protocols.[10,11] Iglesia et al.[12] introduced an *in situ* crystallization approach combining a zeolite gel and ligand-protected metal ions to produce a single zeolite crystal with metal cluster encapsulation. Egeblad et al.[13] reported the synthesis of a single silicalite-1 crystal with encapsulated gold NPs using a NP-modified amorphous silica source. Until now, little success has been achieved in constructing functional hierarchical aggregated zeolite nanostructures. This is because it is very difficult to simultaneously control the growth of zeolites and the properties of the guest species in terms of, e.g., particle size and dispersion. It has been shown that the particles with nanoscale size (<10 nm) and the tailored hierarchical nanostructures can lead to an enhanced performance in the catalysis field.[14−18] Thus, it remains a great challenge to synthesize zeolite materials with the desired functions and tailored structure through a reproducible and flexible method.

We developed a reproducible *in situ* crystallization route to synthesize ZSM-5 microspheres with a magnetic function, good structural stability, and high surface area. To our knowledge, this is the first report on constructing this unique zeolite with aggregated ZSM-5 nanorods (NRs) and well-dispersed uniform $Fe_3O_4$ NPs. Through a nanocasting[19] and *in situ* glycol-ethylene reduction process, uniform $Fe_3O_4$ NPs are confined into pores of the commercially available silica gel (denoted as $Fe_3O_4$@$SiO_2$). In a subsequent hydrothermal treatment, the incomplete dissolution of the $Fe_3O_4$@$SiO_2$ composites at a low alkalinity prevents the escape of $Fe_3O_4$ NPs from silica gel. A high hydrothermal temperature (180 °C) leads to fast crystallization of ZSM-5 nanocrystals. During the growth, $Fe_3O_4$ NPs greatly impact the growth behavior of zeolite crystals, resulting in aggregates of ZSM-5 NRs. This way the uniform $Fe_3O_4$ NPs are well-dispersed at the voids between the crystals, and zeolite crystal aggregation can be controlled. The obtained magnetic microspheres (denoted as $Fe_3O_4$@ZSM-5) possess a relatively uniform size (6−9 $\mu$m), high surface area (340 $m^2/g$), well-designed NR-aggregated shape, and high magnetization (~8.6 emu/g). In particular, the $Fe_3O_4$ NPs exhibit excellent dispensability and good stability which are preferable for heterogeneous catalysis, e.g., the Fischer−Tropsch synthesis (FTS).

A commercial silica gel with an open porous structure (Figure S1) was used in our work. Through a nanocasting and *in situ* glycol-ethylene reduction process, the $Fe_3O_4$@$SiO_2$ composites were obtained. The XRD pattern (Figure S2) shows a broad diffraction peak around 2$\theta$ of 23° assigned to amorphous silica and the sharp diffraction peaks associated with $Fe_3O_4$ NPs (JCPDS no. 19-629), indicating magnetic NPs are formed. After

**Received:** September 16, 2012
**Published:** January 3, 2013

   dx.doi.org/10.1021/ja309194z | *J. Am. Chem. Soc.* 2013, 135, 1181−1184

a hydrothermal treatment, the SEM image (Figures 1a, S3a) of the $Fe_3O_4$@ZSM-5 composite with a Si/Fe molar ratio of 11 (from ICP results) shows a typically spherical morphology with a relatively uniform size of 6−9 $\mu$m in diameter. Field-emission SEM image (FESEM) (Figure 1b) shows that the sphere's surface is composed of many NR-like ZSM-5 crystals. Moreover, the cross-section SEM image (Figure 1c) reveals that the $Fe_3O_4$@ZSM-5 microsphere is composed of numerous concentrically aggregated NRs. The XRD pattern of the $Fe_3O_4$@ZSM-5 composite (Si/Fe = 11) (Figure S4a) reveals that the hybrid material contains $Fe_3O_4$ NPs as well as ZSM-5 zeolite crystals (MFI structure type), indicating a high crystallinity. The TEM image (Figure 1d) of a microsphere edge shows that the ZSM-5 NRs aggregate together, and many tiny NPs are dispersed between these NRs. The HRTEM image (Figure 1d inset) of the cracked microsphere samples shows that lattice fringes with *d*-spacing of 0.48 nm are well-matched to the $d_{111}$ value of the $Fe_3O_4$ NPs and *d*-spacing of ~1 nm to the $d_{200}$ value of ZSM-5 crystal, respectively. These results clearly suggest that $Fe_3O_4$ NPs are located at voids between the ZSM-5 crystals and supported on the NRs. The SEM image of a cracked microsphere sample, combined with EDX elemental mappings (Figure S3b−d), shows that the iron element is well dispersed, indicating that $Fe_3O_4$ NPs exist in the microspheres. $N_2$ adsorption isotherms of the $Fe_3O_4$@ZSM-5 sample (Si/Fe = 11) (Figure S5A) exhibit a sharp uptake at a low relative pressure ($P/P_0$), indicating that the microspheres possess main microporosity. At higher relative pressures, a modest hysteresis loop is observed, suggesting that the microspheres contain a low mesoporosity. The BET surface area and total pore volume are calculated to be ~340 $m^2/g$ and 0.19 $cm^3/g$, respectively. The pore size distribution (Figure S5A inset) indicates the existence of a uniform micropore size distribution at ~0.86 nm and a wide mesopore size distribution, demonstrating that the original microporosity from ZSM-5 and the mesoporosity ascribed to the agglomeration of NRs.

Several parameters can impact the morphology of the final material. If the same silica gel without $Fe_3O_4$ NPs is used for the preparation under the same condition, XRD patterns (Figure S4b) suggest that a well-defined ZSM-5 phase can also be formed. Despite being about the same size (~9 $\mu$m), only intergrown coffin-shaped ZSM-5 crystals are observed (Figure S6). No spherical product is formed, and every crystal is a type of single crystal, suggesting that the existence of $Fe_3O_4$ NPs has a significant impact on ZSM-5 crystallization behavior. Thus, $Fe_3O_4$ NPs are the prerequisite for the formation of such unique magnetic microspheres. Based on the silica gel pore volume, $Fe_3O_4$ loading can also be adjusted. SEM images of the samples $Fe_3O_4$@ZSM-5 (Si/Fe = 22 and 6) (Figure S7a,b) exhibit that hybrids still have spherical morphology of about the same size as the sample with Si/Fe = 11. Also, at a higher alkalinity ($OH^-/Si$ = 0.35), ZSM-5 NRs (Figure S7c) become loosely aggregated, and uniform microspheres cannot be obtained. While iron loading can be varied without compromising sphere quality, the low alkalinity is also crucial in obtaining uniform spherical morphology.

To elucidate the evolution of the $Fe_3O_4$@ZSM-5 microspheres, products were collected at different reaction time intervals. At first, the $Fe_3O_4$@$SiO_2$ composites morphology is similar to that of the initial silica gel with a polyhedral shape (Figure 2a,b). The STEM image of $Fe_3O_4$@$SiO_2$ composite combined with EDX elemental mappings (Figure S8a−c) reveals that the iron element is well dispersed in the matrix of silica gels. A lattice fringe (Figure 2c) with a *d*-spacing of ~0.25 nm can be

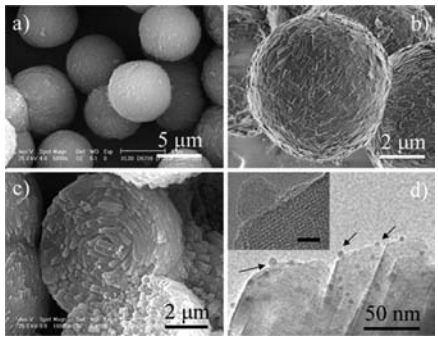


**Figure 1.** Obtained $Fe_3O_4$@ZSM-5 (Si/Fe = 11) microspheres: (a) SEM; (b) FESEM of a single microsphere; (c) SEM of a crushed microsphere; (d) TEM of a microsphere edge. Inset (d) HRTEM image of the $Fe_3O_4$ NP around a ZSM-5 NR (scale bar = 5 nm).

well matched to the $d_{311}$ value of $Fe_3O_4$ crystals. Results suggest that $Fe_3O_4$ NPs are successfully confined within the silica gels. After a 3 h hydrothermal treatment, the amorphous silica gel is partially crystallized into aggregated zeolite particles. The sample's morphology does not change compared with that of the initial silica gel (Figure 2d). However, high-magnification SEM and TEM images (Figure 2e,f) show that the samples are composed of very small particles, suggesting that the material is rearranged, also confirmed by the XRD results (Figure S9, relative ZSM-5 crystallinity is 50%). Meanwhile, iron element is well-dispersed among these particles (Figure S10a−c). When the hydrothermal time is prolonged to 6 h, the sample is completely composed of sphere-like species with a size of 6−9 $\mu$m (Figures 2g, S11a). On its surface, some rectangular sharp edges are observed (Figure 2h), implying that crystal-like domains appear. The corresponding TEM image and SAED pattern also confirm this transformation (Figure S10f), where its internal part is condensed and solid (Figure 2i) and composed of aggregated ZSM-5 crystals and $Fe_3O_4$ NPs (Figures S9, S10d,e, S12a−c). The relative ZSM-5 crystallinity is 76%, implying that some amorphous domains still exist and that ZSM-5 crystals possess substantial defects. After a 12 h hydrothermal treatment, the size of sphere-like sample does not change obviously (Figures 2j and S11b). However, the morphology of its surface changes significantly (Figure 2k). Some NRs as well as edges and corners appear on the surface, suggesting that the transformation takes place. Its internal part (Figure 2l) does not consist of NRs, indicating that the transformation occurs on the surface at first. The samples possess a good relative crystallinity of a zeolite phase (87%), suggesting that the ZSM-5 crystals further grow. The iron element is still well-dispersed internally in the microsphere (Figure S12d−f). After 24 h of hydrothermal treatment, the microsphere size (Figure 1b) is similar to that of the sample obtained within 6 h (Figure 2g), while the ZSM-5 NRs become relatively uniform, and the edges and corners disappear (Figure 1b) compared to the sample obtained within 12 h reaction (Figure 2k). It is noted that the microspheres are essentially composed of ZSM-5 NRs (relative ZSM-5 crystallinity is 95%), suggesting that the internal also undergoes recrystallization from the surface.

Based on previous observations, an *in situ* crystallization process for the magnetic $Fe_3O_4$@ZSM-5 microspheres is proposed (Figure 3). Commercial mesoporous silica gel is utilized as a host to confine $Fe_3O_4$ NPs (~10 nm) through a nanocasting and *in situ* glycol-ethylene reduction process (Figure 3a). When $Fe_3O_4$@$SiO_2$ composite is used as a silica source for


dx.doi.org/10.1021/ja309194z | *J. Am. Chem. Soc.* 2013, 135, 1181−1184

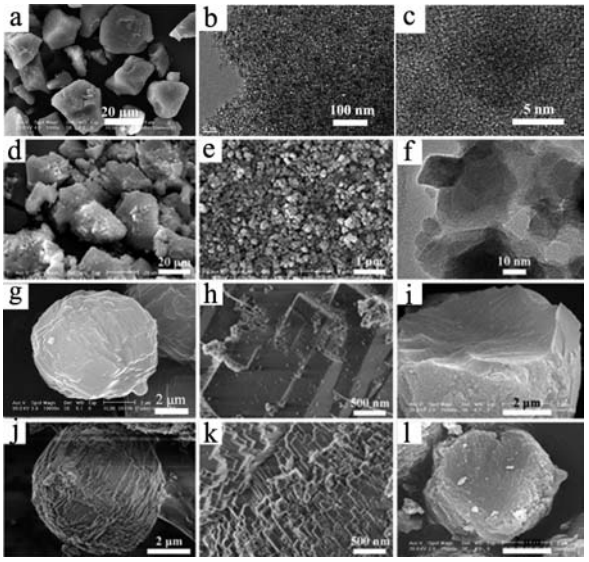


**Figure 2.** (a) SEM and (b) TEM of $Fe_3O_4$@$SiO_2$ composites; (c) HRTEM of $Fe_3O_4$ NPs in the silica gel; (d,e) SEM of samples after 3 h growth at different magnifications and corresponding TEM image (f); (g,h) SEM of sphere-like particles after 6 h hydrothermal treatment at different magnifications and (i) SEM of crushed samples; (j,k) SEM of sphere-like particles after 12 h hydrothermal treatment at different magnifications and(l) SEM of crushed samples.

zeolite growth, the dissolution of the retaining structure is inhibited at a low alkaline ($OH^-$/Si = 0.25) condition, which in turn prevents the $Fe_3O_4$ NPs escape from the silica gel. A high-temperature hydrothermal treatment for a short time leads to a fast nucleation of ZSM-5 nanocrystals (Figure 3b). Simultaneously, these numerous ZSM-5 nanocrystals aggregate together with $Fe_3O_4$ NPs at a low alkaline condition, leading to the formation of a spherical solid particle with the least surface free energy as a result of the Curie−Wulff law,[20] illustrating a kinetic-controlled aggregation. With the reaction time increases, the crystal growth of zeolites is predominate, and the crystallinity greatly increases (from 50 to 76%), which often produces the solid spheres with a symmetric polyhedral morphology.[22] However, in this stage the crystallinity of the zeolite crystals is not high, the solid microspheres contain a large number of structural defects, which can accommodate the $Fe_3O_4$ NPs into an integral spherical particle. As the hydrothermal reaction progresses and the aluminosilicate species in solution are almost consumed, a recrystallization process is predominate, i.e., preferentially the surface zeolite nanocrystals are recrystallized into some single crystalline domains.[20] Thus the surface of the microspheres is rough and exhibits some angularities (Figure 3c). During this process, the crystallinity of zeolite crystals further increases (87%). Normally, the single crystalline domains could extend on the surface, and the crystals are further grown to form large ones via an Ostwald ripening process.[20−23] In our synthetic condition, the ZSM-5 crystal growth may be suppressed by the well-dispersed $Fe_3O_4$ NPs because these NPs are so large (∼ 10 nm) and cannot be involved in the crystallinity of zeolites and encapsulated in a single-crystal of ZSM-5. Hence, the crystallization of zeolites may favor to occur around them, and the sphere-like particles recrystallize to form the NRs first on the surface during the ripening growth process (Figure 3d).[11,20−23] As the reaction proceeds, this thin ZSM-5 NR shell increases its thickness and extends inward to the core of the spherical particle until the overall NRs are formed completely. The materials become more spherical and thus more stable, eliminating edges and corners formed on the surface of the spherical $Fe_3O_4$@ZSM-5 composites (Figure 3e). The microspheres undergo a recrystallization process from surface to core to possess a high-crystalline zeolite and a good dispersion of $Fe_3O_4$ NPs.

$Fe_3O_4$ NPs can endow a magnetic function to the ZSM-5 microspheres, which makes them easy to separate. After calcination in air to remove organic species, the Raman spectrum result (Figure S13) shows that the iron oxide in the microspheres is composed of both $Fe_3O_4$ and $\gamma$-$Fe_2O_3$, implying that $Fe_3O_4$ NPs are partially oxidized to $\gamma$-$Fe_2O_3$. The iron oxide content is ∼17 wt %, the saturation value of the iron oxide@ZSM-5 (Si/Fe = 6) (Figure S5B,a) can reach as high as 8.6 emu/g (normalized to the weight of composites). The saturation magnetization values for iron oxide@ZSM-5 (Si/Fe = 11 and 22) are 3.3 and 1.5 emu/g, respectively (Figure S5B,b,c), decreasing with the increase of Si/Fe ratio. Importantly, the magnetic hysteresis loops prove that the composites inherit a superparamagnetic property. It is advantageous that no magnetization remains when the applied magnetic field is removed. The catalytic performance of the iron oxide@ZSM-5 is measured for the acetalization of cyclohexanone with methanol. The microsphere catalyst shows a high conversion of 95%, and the selectivity toward 1,1-dimethoxycyclohexane is 100%. The zeolite microsphere catalysts are easily recovered by a magnet from the reaction solution and exhibit a similar performance even after running for more than six cycles (Figure S14).

This kind of $Fe_3O_4$@ZSM-5 composite can also be regarded as a type of zeolite-supported iron catalyst. Here we take the FTS as a probe to investigate the catalytic performance. Before the catalytic test, the $Fe_3O_4$@ZSM-5 composites were calcined in air and ion exchanged to H form. The morphology and structure of the composites did not change (Figures S15, S16). Thereafter, the catalyst was *in situ* reduced by 5% $H_2$/Ar and activated according to a previous process.[17,18] Conversion of CO (Figure S17a) on the $Fe_3O_4$@ZSM-5 (Si/Fe = 11) is observed to increase at the beginning, demonstrating an activated stage in FTS on these catalysts. After ∼60 h on stream, CO conversion reaches the steady state at ∼87%. After 110 h, CO conversion does not decline, suggesting an excellent stability. This may be due to the confinement effect by ZSM-5 microspheres on the small $Fe_3O_4$ NPs.

The selectivity toward $C_5$−$C_{12}$ could be as high as 44.6% (Figure S17b) due to the size of NPs.[18] Moreover, only a small amount of $C_{13}$−$C_{20}$ (3.2%) can be formed, and no $C_{20+}$ hydrocarbons are detected, indicating selectivity of heavier

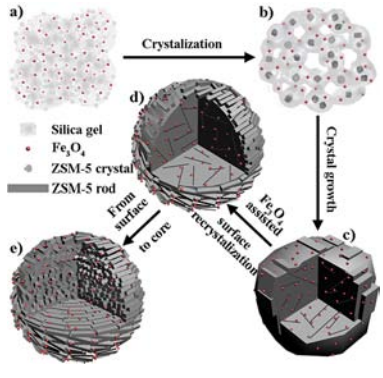


**Figure 3.** The formation mechanism of functional $Fe_3O_4$@ZSM-5 microspheres through an *in situ* crystallization from surface to core.


dx.doi.org/10.1021/ja309194z | J. Am. Chem. Soc. 2013, 135, 1181−1184

products is suppressed. The selectivity of $CH_4$ is relatively higher (16%) as compared to most Fe-based catalysts. In terms of Fe-based catalysts, Fe carbides are the active species as CO dissociation occurring on these sites,[18,24] even though $Fe_3O_4$, Fe metal, or surface iron phases are reported to be the active species for FTS.[25] So prior to reaching the best catalytic activities, it is first activated in syngas. For comparison, selectivity for $C_5-C_{12}$ is ~36% over the physical mixed catalyst of $Fe_3O_4$ NPs and ZSM-5 (Table S1). Compared with other Fe-zeolite-based FTS catalysts, our $Fe_3O_4$@ZSM-5 microsphere catalysts also show a better $C_5-C_{12}$ selectivity as a promoter-free catalyst. Usually, some promoters are added into Fe-based catalysts to decrease the $CH_4$ selectivity.[26] However in our work, no promoters are added, resulting in relatively high methane selectivity. The effect of zeolites on the selectivity to different hydrocarbons has been reported in the literature.[27,28] The zeolite acid sites play an important role in cracking of heavier hydrocarbons, leading to good selectivity of gasoline products in FTS.

In conclusion, we demonstrate a reproducible *in situ* crystallization route to synthesize uniform $Fe_3O_4$@ZSM-5 microspheres with aggregated-ZSM-5 NRs and well-dispersed uniform $Fe_3O_4$ NPs. The obtained samples possess a relatively uniform size (6–9 $\mu$m), high surface area, well-designed NR-aggregated shape, ultrafine $Fe_3O_4$ NPs, and high magnetization (~ 8.6 emu/g). We propose a NP-assisted recrystallization process from surface to core for the formation of such unique $Fe_3O_4$@ZSM-5 microspheres. Moreover, the obtained microspheres show excellent catalytic performance in FTS. The CO conversion on the $Fe_3O_4$@ZSM-5 (Si/Fe = 11) can reach 87% and remain at least 110 h, and selectivity toward $C_5-C_{12}$ is as high as 44.6%. This *in situ* crystallization route could be extended to synthesize other metal oxide-zeolite composites with unique nanostructure, e.g., NiO@zeolite or $Co_3O_4$@zeolite. Most importantly, in possessing magnetic property, the $Fe_3O_4$@ZSM-5 composite material allows for practical handling, e.g., in magnetically stabilized beds to reduce catalyst losses.

## ■ ASSOCIATED CONTENT

### Ⓢ Supporting Information

Experimental details and characterization data. This material is available free of charge via the Internet at http://pubs.acs.org.

## ■ AUTHOR INFORMATION


### Corresponding Author

dyzhao@fudan.edu.cn


### Notes

The authors declare no competing financial interest.

## ■ ACKNOWLEDGMENTS

This work was supported by NSF of China (20890123, 21073043, 21210004), State Key Basic Research Program of the PRC (2009AA033701, 2009CB930400), Science and Technology Commission of Shanghai Municipality (08DZ2270500, 10JC1401800), and Shanghai Leading Academic Discipline Project (B108). Partial support from Australian Research Council Discovery Project (DP0986192) and Australian Endeavour Executive Award for M.D.

## ■ REFERENCES


(1) (a) Corma, A. *Chem. Rev.* **1997**, *97*, 2373. (b) Qian, X. F.; Li, B.; Hu, Y. Y.; Niu, G. X.; Zhang, D. Y. H.; Che, R. C.; Tang, Y.; Su, D. S.; Asiri, A. M.; Zhao, D. Y. *Chem.—Eur. J.* **2012**, *18*, 931.

(2) (a) Varoon, K.; Zhang, X.; Elyassi, B.; Brewer, D. D.; Gettel, M.; Kumar, S.; Lee, J. A.; Maheshwari, S.; Mittal, A.; Sung, C.-Y.; Cococcioni, M.; Francis, L. F.; McCormick, A. V.; Mkhoyan, K. A.; Tsapatsis, M. *Science* **2011**, *334*, 72. (b) Chen, H.; Wydra, J.; Zhang, X.; Lee, P.-S.; Wang, Z.; Fan, W.; Tsapatsis, M. *J. Am. Chem. Soc.* **2011**, *133*, 12390. (c) Yoo, W. C.; Stoeger, J. A.; Lee, P.-S.; Tsapatsis, M.; Stein, A. *Angew. Chem., Int. Ed.* **2010**, *49*, 8699. (d) Lee, P. S.; Zhang, X.; Stoeger, J. A.; Malek, A.; Fan, W.; Kumar, S.; Yoo, W. C.; Al Hashimi, S.; Penn, R. L.; Stein, A.; Tsapatsis, M. *J. Am. Chem. Soc.* **2011**, *133*, 493. (e) Duke, M. C.; O'Brien-Abraham, J.; Milne, N.; Zhu, B.; Lin, J. Y. S.; Diniz da Costa, J. C. Sep. *Purif. Technol.* **2009**, *68*, 343. (f) Fan, W.; Snyder, M. A.; Kumar, S.; Lee, P.-S.; Yoo, W. C.; McCormick, A. V.; Lee Penn, R.; Stein, A.; Tsapatsis, M. *Nat. Mater.* **2008**, *7*, 984. (g) Jia, C. J.; Liu, Y.; Schmidt, W.; Lu, A. H.; Schüth, F. *J. Catal.* **2010**, *269*, 71. (h) Cundy, C. S.; Cox, P. A. *Chem. Rev.* **2003**, *103*, 663. (i) Zhu, B.; Zou, L.; Doherty, C. M.; Hill, A. J.; Lin, Y. S.; Hu, X.; Wang, H.; Duke, M. *J. Mater. Chem.* **2010**, *20*, 4675. (j) Ge, Q.; Wang, Z.; Yan, Y. *J. Am. Chem. Soc.* **2009**, *131*, 17056. (k) Wang, Z.; Ge, Q.; Shao, J.; Yan, Y. *J. Am. Chem. Soc.* **2009**, *131*, 6910. (l) Lew, C. M.; Cai, R.; Yan, Y. *Acc. Chem. Res.* **2010**, *43*, 210.

(3) Kim, Y. I.; Keller, S. W.; Krueger, J. S.; Yonemoto, E. H.; Saupe, G. B.; Mallouk, T. E. *J. Phys. Chem. B* **1997**, *101*, 2491.

(4) Yonemoto, E. H.; Kim, Y. I.; Schmehl, R. H.; Wallin, J. O.; Shoulders, B. A.; Richardson, B. R.; Haw, J. F.; Mallouk, T. E. *J. Am. Chem. Soc.* **1994**, *116*, 10557.

(5) Brigham, E. S.; Snowden, P. T.; Kim, Y. I.; Mallouk, T. E. *J. Phys. Chem.* **1993**, *97*, 8650.

(6) Mukadam, M. D.; Yusuf, S. M.; Sasikala, R. *J. Appl. Phys.* **2007**, *102*, 103902.

(7) Djakovitch, L.; Koehler, K. *J. Am. Chem. Soc.* **2001**, *123*, 5990.

(8) Jie, D.; Zhenghe, X.; Steven, M. K. *Adv. Funct. Mater.* **2009**, *19*, 1268.

(9) Bourlinos, A. B.; Zboril, R.; Petridis, D. *Microporous Mesoporous Mater.* **2003**, *58*, 155.

(10) Zhan, B. Z.; Iglesia, E. *Angew. Chem., Int. Ed.* **2007**, *46*, 3697.

(11) Shan, W.; Yu, T.; Wang, B.; Hu, J.; Zhang, Y.; Wang, X.; Tang, Y. *Chem. Mater.* **2006**, *18*, 3169.

(12) Choi, M.; Wu, Z.; Iglesia, E. *J. Am. Chem. Soc.* **2010**, *132*, 9129.

(13) Anders B, L.; Karen T, H.; Lars F, L.; Søren B, S.; Stig, H.; Ferdi, S.; Michael, P.; Jan-Dierk, G.; Søren, K.; Claus H, C.; Kresten, E. *Angew. Chem., Int. Ed.* **2010**, *49*, 3504.

(14) Song, H.; Rioux, R. M.; Hoefelmeyer, J. D.; Komor, R.; Niesz, K.; Grass, M.; Yang, P.; Somorjai, G. A. *J. Am. Chem. Soc.* **2006**, *128*, 3027.

(15) Tsung, C.-K.; Kuhn, J. N.; Huang, W.; Aliaga, C.; Hung, L.-I.; Somorjai, G. A.; Yang, P. *J. Am. Chem. Soc.* **2009**, *131*, 5816.

(16) Li, W.; Deng, Y.; Wu, Z.; Qian, X.; Yang, J.; Wang, Y.; Gu, D.; Zhang, F.; Tu, B.; Zhao, D. Y. *J. Am. Chem. Soc.* **2011**, *133*, 15830.

(17) Chen, W.; Fan, Z.; Pan, X.; Bao, X. *J. Am. Chem. Soc.* **2008**, *130*, 9414.

(18) Yu, G.; Sun, B.; Pei, Y.; Xie, S.; Yan, S.; Qiao, M.; Fan, K.; Zhang, X.; Zong, B. *J. Am. Chem. Soc.* **2010**, *132*, 935.

(19) Yang, H.; Zhao, D. Y. *J. Mater. Chem.* **2005**, *15*, 1217.

(20) Chen, X.; Qiao, M.; Xie, S.; Fan, K.; Zhou, W.; He, H. *J. Am. Chem. Soc.* **2007**, *129*, 13305.

(21) Yao, J. F.; Li, D.; Zhang, X. Y.; Kong, C. H.; Yue, W. B.; Zhou, W. Z.; Wang, H. T. *Angew. Chem., Int. Ed.* **2008**, *47*, 8397.

(22) Greer, H.; Wheatley, P. S.; Ashbrook, S. E.; Morris, R. E.; Zhou, W. *J. Am. Chem. Soc.* **2009**, *131*, 17986.

(23) Zhou, W. *Adv. Mater.* **2010**, *22*, 3086.

(24) Sudsakorn, K.; Goodwin, J. G., Jr; Adeyiga, A. A. *J. Catal.* **2003**, *213*, 204.

(25) Mansker, L. D.; Jin, Y.; Bukur, D. B.; Datye, A. K. *Appl. Catal., A* **1999**, *186*, 277.

(26) Zhang, Q.; Kang, J.; Wang, Y. *ChemCatChem* **2010**, *2*, 1030.

(27) Martínez, A.; López, C. *Appl. Catal., A* **2005**, *294*, 251.

(28) Kang, S. H.; Bae, J. W.; Woo, K. J.; Sai Prasad, P. S.; Jun, K. W. *Fuel Process. Technol.* **2010**, *91*, 399.